TU Delft

Delft University of Technology

Kinetic-arrest-induced phase coexistence and metastability in (Mn,Fe)2(P,Si)

Miao, X. F.; Mitsui, Y.; Dugulan, A. Iulian; Caron, L.; Thang, N. V.; Manuel, P.; Koyama, K.; Takahashi, K.; Van Dijk, N. H.; Brück, E.

DOI
10.1103/PhysRevB.94.094426

Publication date
2016

Document Version
Final published version

Published in
Physical Review B (Condensed Matter and Materials Physics)

Citation (APA)
Miao, X. F., Mitsui, Y., Dugulan, A. I., Caron, L., Thang, N. V., Manuel, P., Koyama, K., Takahashi, K., Van Dijk, N. H., & Brück, E. (2016). Kinetic-arrest-induced phase coexistence and metastability in (Mn,Fe)2(P,Si). *Physical Review B (Condensed Matter and Materials Physics)*, *94*(9), Article 094426. https://doi.org/10.1103/PhysRevB.94.094426

Important note
To cite this publication, please use the final published version (if applicable).
Please check the document version above.

Copyright
Other than for strictly personal use, it is not permitted to download, forward or distribute the text or part of it, without the consent of the author(s) and/or copyright holder(s), unless the work is under an open content license such as Creative Commons.

Takedown policy
Please contact us and provide details if you believe this document breaches copyrights.
We will remove access to the work immediately and investigate your claim.

This work is downloaded from Delft University of Technology.
For technical reasons the number of authors shown on this cover page is limited to a maximum of 10.

Kinetic-arrest-induced phase coexistence and metastability in $(Mn,Fe)_2(P,Si)$

X. F. Miao,[1,*] Y. Mitsui,[2] A. Iulian Dugulan,[1] L. Caron,[1,3] N. V. Thang,[1] P. Manuel,[4] K. Koyama,[2] K. Takahashi,[5] N. H. van Dijk,[1] and E. Brück[1]

[1]*Fundamental Aspects of Materials and Energy, Faculty of Applied Sciences, Delft University of Technology, Mekelweg 15, 2629 JB Delft, The Netherlands*

[2]*Graduate School of Science and Engineering, Kagoshima University, 1-21-35, 890-0065, Kagoshima, Japan*

[3]*Max Planck Institute for Chemical Physics of Solids, Nöthnitzer Straße 40, D-01187 Dresden, Germany*

[4]*ISIS facility, Rutherford Appleton Laboratory, Chilton, Didcot, Oxfordshire, OX11 0QX, United Kingdom*

[5]*High Field Laboratory for Superconducting Materials, Institute for Materials Research, Tohoku University, 980-857, Sendai, Japan*

(Received 14 June 2016; revised manuscript received 8 September 2016; published 22 September 2016)

Neutron diffraction, Mössbauer spectroscopy, magnetometry, and in-field x-ray diffraction are employed to investigate the magnetoelastic phase transition in hexagonal $(Mn,Fe)_2(P,Si)$ compounds. $(Mn,Fe)_2(P,Si)$ compounds undergo for certain compositions a second-order paramagnetic (PM) to a spin-density-wave (SDW) phase transition before further transforming into a ferromagnetic (FM) phase via a first-order phase transition. The SDW-FM transition can be kinetically arrested, causing the coexistence of FM and untransformed SDW phases at low temperatures. Our in-field x-ray diffraction and magnetic relaxation measurements clearly reveal the metastability of the untransformed SDW phase. This unusual magnetic configuration originates from the strong magnetoelastic coupling and the mixed magnetism in hexagonal $(Mn,Fe)_2(P,Si)$ compounds.

DOI: 10.1103/PhysRevB.94.094426

I. INTRODUCTION

First-order magnetic phase transitions in magnetic materials bring a variety of interesting phenomena such as giant magnetocaloric effect [1–3], colossal (or giant) magnetoresistance effect [4,5], and magnetic shape memory effect [6]. The first-order phase transition is characterized by a discontinuous change in the first derivative of the free energy (e.g., magnetization M, entropy S, and volume V) triggered by thermodynamic variables (e.g., temperature T, magnetic field H, and pressure P). Intrinsic composition disorder broadens the first-order phase transition, causing a coexistence of transformed and untransformed phases over the phase transition region, as indicated by different nano- and microscale techniques [7–12]. After crossing the phase transition region, the system reaches an equilibrium state with a homogeneous phase.

Under certain conditions, the first-order phase transition can be kinetically arrested, i.e., the phase coexistence remains beyond the phase transition region. An example of this behavior is reported for doped $CeFe_2$ alloys [13–15]. When $Ce(Fe_{0.96}Ru_{0.04})_2$ is cooled in an appropriate magnetic field, crossing the first-order ferromagnetic (FM) to antiferromagnetic (AFM) transition, the nucleation and growth of the low-T AFM phase is found to be hindered. As a result, a small fraction of the untransformed FM phase is frozen randomly in the stable AFM matrix at temperatures well below the Néel temperature T_N [13]. The supercooled FM phase is energetically metastable, which will be de-arrested and transformed to the stable AFM phase by thermal fluctuations.

A similar phenomenon has been reported in diverse classes of magnetic systems, such as Gd_5Ge_4 [16], Ni-Mn-X based Heusler alloys [17–19], doped-FeRh [20], Nd_7Rh_{13} [21], Tb_4LuSi_3 [22], and manganites [23–27]. The kinetically arrested phase transition is associated with a strong magnetostructural coupling in these magnetic systems. For instance, the high-T FM to low-T AFM transition in doped-$CeFe_2$ alloys [13,14] is coupled with a cubic to rhombohedral structural transformation, while the high-T AFM to low-T FM transition in Gd_5Ge_4 [16] is accompanied by the Sm_5Ge_4-type orthorhombic to Gd_5Si_4-type orthorhombic structural transition.

Recent studies [28] on hexagonal $(Mn,Fe)_2(P,Si)$-type compounds show the coexistence of FM and incommensurate magnetic phases at temperatures far below the critical temperature (T_C) for the formation of the ferromagnetic phase. Höglin *et al.* [28] proposed that the phase coexistence in $(Mn,Fe)_2(P,Si)$ originates from a phase segregation in the paramagnetic (PM) state. The sample consists of two phases with slightly different lattice parameters in the high-temperature PM state [28]. These two phases transform into a FM and an incommensurate magnetic phase upon cooling [28]. However, theoretical calculations revealed that the coexistence of a FM and an incommensurate magnetic phase may be a result of competing magnetic configurations [29,30]. The incommensurate magnetic phase is considered to be an intermediate metastable phase, which is formed due to the kinetic arrest of the PM-FM transition [30].

In the present work, the phase coexistence and metastability in $(Mn,Fe)_2(P,Si)$-type compounds has been investigated using a combination of neutron diffraction, magnetometry, Mössbauer spectroscopy, and in-field x-ray diffraction. This provides further insight into the magnetoelastic coupling and mixed magnetism in $(Mn,Fe)_2(P,Si)$-type compounds. Our study also helps to extend the understanding of the kinetic arrest in magnetic systems showing a first-order phase transition.

II. EXPERIMENT

Polycrystalline samples with nominal compositions $MnFe_{0.95}P_{0.67}Si_{0.33}$ (hereafter referred to as "S0"), $Mn_{1.30}Fe_{0.65}P_{0.67}Si_{0.33}$ ("S1"), $MnFe_{0.95}P_{0.71}Si_{0.29}$ ("S2"), and

*x.f.miao@tudelft.nl

 ©2016 American Physical Society

$MnFe_{0.95}P_{0.67}Si_{0.33}N_{0.02}$ ("S3") samples were prepared from Mn, Fe, Fe_3N, red-P, and Si powders as described earlier [31]. Neutron diffraction experiments were performed on the WISH [32] time-of-flight diffractometer at the ISIS Facility, Rutherford Appleton Laboratory, UK. The powdered sample of about 6 g was put into a vanadium can mounted in a helium cryostat. Diffraction data were collected between 200 and 1.5 K upon cooling. The magnetic properties were characterized using a superconducting quantum interference device (SQUID) magnetometer (Quantum Design MPMS 5XL). In magnetic measurements, powder samples were put into a capsule, which was mounted in a plastic straw with a diamagnetic contribution of the order of 10^{-5} A m^2 in 1 T. The powders were compacted to avoid reorientation. X-ray powder diffraction experiments using Cu $K\alpha$ radiation were performed at 300 and 10 K in magnetic fields up to 5 T [33]. Structure refinement of the x-ray and neutron diffraction patterns was performed using the Rietveld method implemented in the Fullprof package [34]. In all samples, about 1 wt.% $(Mn,Fe)_3Si$ impurity phase was detected in the x-ray patterns. Our previous studies show that the $(Mn,Fe)_3Si$ phase shows an antiferromagnetic transition [35]. The magnetic signal from the $(Mn,Fe)_3Si$ impurity phase is two orders of magnitude weaker than that from the main phase, which has a negligible influence on the magnetic results. Transmission ^{57}Fe Mössbauer experiments at 300 K were performed on a spectrometer using a ^{57}Co(Rh) source with a constant acceleration, while the Mössbauer experiments at 4.2 K were on a spectrometer with a sinusoidal velocity transducer. The velocity calibrations were carried out using an α-Fe foil at room temperature. The source and the absorbing samples were kept at the same temperature during the measurements. The Mössbauer spectra were fitted using the Mosswinn 4.0 program [36].

III. RESULTS AND DISCUSSION

A. Magnetization measurements

Figure 1(a) shows the temperature-dependent magnetization (M) of the as-prepared S0 during the first two cooling and warming cycles. A lower T_C upon the first cooling than on the second cooling is due to the "virgin effect", which is a common feature in $(Mn,Fe)_2(P,Si)$-type compounds [37]. The observed pronounced thermal hysteresis marks the strong first-order nature of the PM-FM phase transition in S0. After two cooling and warming cycles, M-H curves were measured isothermally at 5 K. The M-H curves in Fig. 1(b) show a characteristic soft-ferromagnetic response with a saturation magnetization (M_s) of about 155 A m^2 kg^{-1} at 5 K, which is consistent with previous reports [38].

Our previous studies reveal that the T_C and the thermal hysteresis of the $(Mn,Fe)_2(P,Si)$-type compounds can be tuned directly by varying the Mn/Fe ratio [39]. With an increase in Mn/Fe ratio from 1.00/0.95 to 1.30/0.65, a rapid decrease in T_C and a reduction in thermal hysteresis is observed in Fig. 1(c). Additionally, the increase in the Mn/Fe ratio causes an unexpected and significant drop in the magnetization below T_C. As presented in Fig. 1(c), the PM-FM transition is complete at about 60 K for the second cooling. As a result, S1 is expected to be at a pure FM state below 60 K. However, the isothermal M-H curve [Fig. 1(d)] measured at 5 K after the second cooling shows an unexpected metamagnetic transition when the field is applied for the first time. Below 1 T, the M-H curve shows a ferromagnetlike feature. Beyond 1 T, a metamagnetic transition appears and is completed at about 4 T. The decreasing-field curve does not show the reverse metamagnetic transition, nor does the subsequent increasing-field curve show any signature of the metamagnetic transition. Consequently, the initial magnetic state is not recovered after the first increase and decrease in field, suggesting the metastability of the initial magnetic state after cooling.

A similar phenomenon has been observed in a wide compositional range of $(Mn,Fe)_2(P,Si)$-type compounds. For instance, a metamagnetic transition is also present in the isothermal M-H curves of S2 [Fig. 2(b)] and S3 [see Fig. 2(d)], although the transition is still incomplete up to 5 T. Such anomalies have been observed in a variety of magnetic materials, and originate from incomplete first-order phase transition caused by kinetic arrest [17,24,40]. One predominant consequence of the kinetic-arrest effect is the

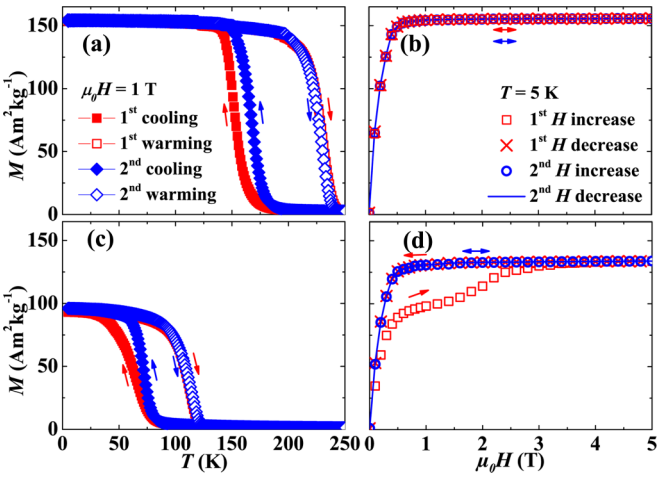

FIG. 1. M-T and M-H plots for S0 (a) and (b) and S1 (c) and (d).

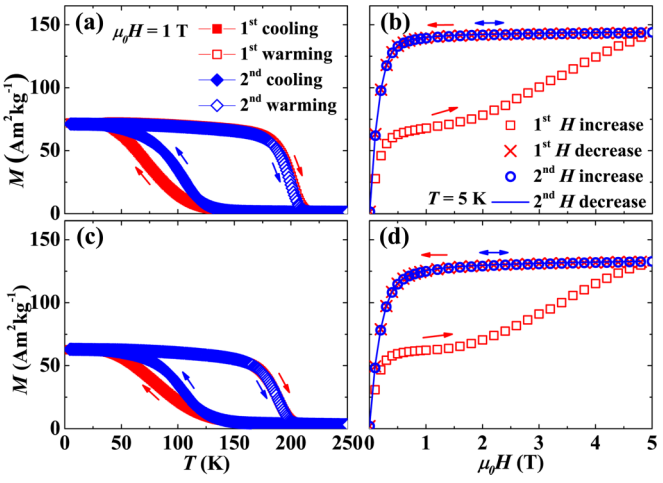

FIG. 2. M-T and M-H plots for the as-prepared S2 (a) and (b), and S3 (c) and (d).

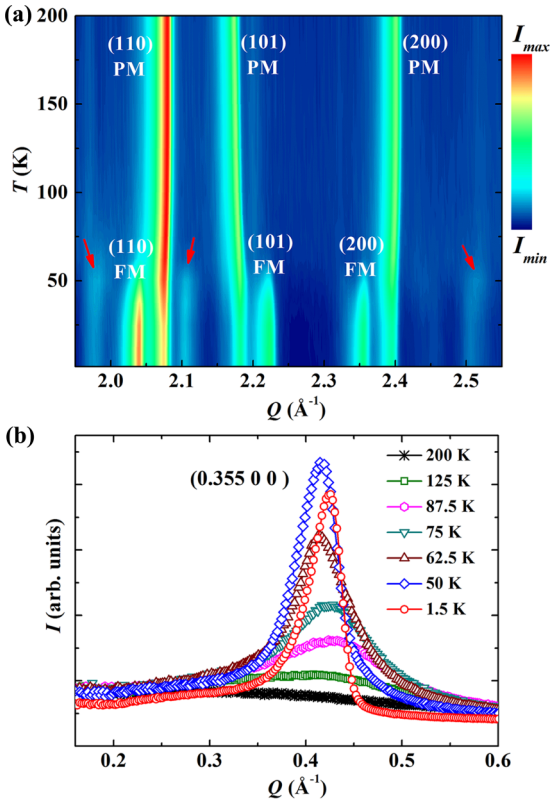

FIG. 3. (a) Contour plot of the neutron diffraction patterns collected at WISH (detector bank 5 with $\langle 2\theta \rangle \approx 152.83°$) for S1. The intensity is on a logarithmic scale. (b) The (0.355 0 0) magnetic reflection of the SDW phase at different temperatures recorded at WISH (detector bank 1 with $\langle 2\theta \rangle \approx 27.08°$).

coexistence of transformed and untransformed phases at temperatures far below the phase-transition temperature. Our neutron diffraction (Sec. III B) and Mössbauer spectroscopy (Sec. III C) studies provide experimental evidence for this phase coexistence in these $(Mn,Fe)_2(P,Si)$-type compounds.

B. Neutron diffraction

We performed neutron powder diffraction for the as-prepared S1 during cooling from 200 to 1.5 K. The contour plot in Fig. 3(a) shows the temperature dependence of the diffraction pattern in the Q range from 1.95 to 2.55 $Å^{-1}$. At high temperatures, the diffraction peaks correspond to the crystal structure of the PM state, which crystallizes in the hexagonal Fe_2P-type structure (space group $P\bar{6}2m$). No phase separation in the PM state was detected in the neutron diffraction patterns within the resolution. At $T \approx 50$ K, a series of new peaks appear beside the initial high-T peaks. The intensities of these new peaks increase with the decrease in temperature, while the intensities of the initial high-T peaks show the opposite trend. Structure refinement reveals that these new peaks belong to a FM phase with the same crystal structure as the PM phase, but with different lattice parameters. The Fe and Mn magnetic moments in the FM phase lie within the basal plane with magnitudes of 1.5 and 2.8 μ_B, respectively. The structural details of the FM phase derived from Rietveld refinement are summarized in Table I. The refined ratio of

TABLE I. Structural parameters of the as-prepared S1 at 1.5 K derived from neutron diffraction. Space group: $P\bar{6}2m$. Atomic positions: $3f(x_1,0,0)$, $3g(x_2,0,1/2)$, $2c(1/3,2/3,0)$, and $1b(0,0,1/2)$.

	Parameters	FM	SDW
	Fraction (%)	47.4(2)	52.6(2)
	a (Å)	6.1586(1)	6.0582(1)
	c (Å)	3.3304(1)	3.4421(1)
	V (Å^3)	109.394(4)	109.405(5)
$3f$	x_1	0.2601(3)	0.2581(3)
	n(Fe)/n(Mn)	0.165/0.085(1)	0.165/0.085(1)
	M (μ_B)	1.5(1)	0.8(2)
$3g$	x_2	0.5965(4)	0.5921(4)
	n(Mn)/n(Fe)	0.25/0	0.25/0
	M (μ_B)	2.8(1)	3.1(2)
$2c$	n(P)/n(Si)	0.117/0.050(4)	0.117/0.050(4)
$1b$	n(P)/n(Si)	0.050/0.033(4)	0.050/0.033(4)
	R_{Mag} (%)	2.68	8.35
	Rp (%)	4.26	
	wRp (%)	4.90	
	χ^2	7.92	

(Mn+Fe) : (P+Si) is 2:1, which indicates that the expected composition for Fe_2P-based materials is realized. Additionally, some weak satellites around the main Bragg peaks appear at low temperature, as indicated by the arrows in Fig. 3(a), and a Bragg peak at $Q \approx 0.42$ $Å^{-1}$ develops with the decrease in temperature [see Fig. 3(b)]. These peaks cannot be indexed by any nuclear Bragg peaks. This strongly suggests the formation of another magnetic phase at low temperatures. An automatic indexing procedure using the $\boldsymbol{k}$-search program in the Fullprof package [34] was performed to determine the propagation vector $\boldsymbol{k}$ of this magnetic phase. A propagation vector of $\boldsymbol{k} = (0.355(1),0,0)$ is derived, which indicates an incommensurate-magnetic structure. The possible magnetic structures are a helical spin configuration or a spin-density wave, in which the direction or the size of the magnetic moments changes along the propagation direction, respectively. The remaining intensities of the initial high-T peaks are from the nuclear structure of this incommensurate-magnetic phase.

In order to resolve the detailed magnetic structure of this incommensurate-magnetic phase, we performed a representation analysis [41,42] using the BasIreps program in the Fullprof package [34]. Representation analysis yields two nonzero irreducible representations (IRs) for both Fe and Mn moments on the $3f$ and $3g$ sites, respectively. One IR corresponds to both Fe and Mn moments along the c axis, and the other corresponds to both moments within the ab plane. A helical spin configuration with $\boldsymbol{k} = (0.355,0,0)$ is not allowed by the IRs. As a result, the incommensurate-magnetic phase can be described by a sinusoidal spin-density wave (SDW) with $\boldsymbol{k} = (0.355,0,0)$. We fitted the diffraction patterns using different magnetic configurations (see the Appendix). The magnetic structure with the Mn and Fe moments parallel and perpendicular to the $\boldsymbol{k}$, respectively, gives the best fit [see Fig. 4(a)] with a magnetic R factor of 8.4%. A schematic representation of this magnetic structure is presented in

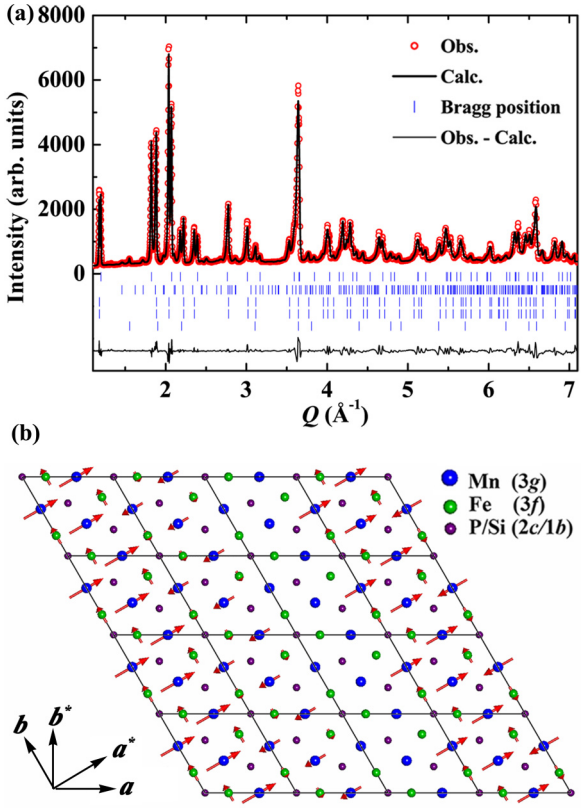

FIG. 4. (a) Fitted powder neutron diffraction pattern for S1 collected at 1.5 K at WISH (detector bank 3 with $\langle 2\theta \rangle \approx 90^\circ$). Vertical lines indicate the peak positions (from top to bottom) for the nuclear structure of the SDW phase, magnetic structure of the SDW phase, nuclear structure of the FM phase, magnetic structure of the FM phase, and the impurity $(Mn,Fe)_3Si$ phase, respectively. (b) Schematic representation (4×4) of magnetic configuration in the basal ab plane for the SDW phase. $\boldsymbol{a}^*$ and $\boldsymbol{b}^*$ are the primitive vectors of the reciprocal lattice. The propagation vector $\boldsymbol{k}$ is along $\boldsymbol{a}^*$. Both the Mn and Fe moments lie within the basal ab plane. The Mn moment is aligned parallel to $\boldsymbol{k}$ and the Fe moment is perpendicular to $\boldsymbol{k}$.

Fig. 4(b). The structure details of the SDW phase derived from the refinement are summarized in Table I. At 1.5 K, S1 consists of FM and SDW phases with weight fractions of about 47.4% and 52.6%, respectively. The FM phase has larger and smaller dimensions in the basal plane and along the c axis, respectively, in comparison with the SDW phase. The site occupancies were constrained to be equal for the FM and SDW phases in the refinement. The Fe moment in the FM phase is almost twice as large as in the SDW phase, while the Mn moment is not significantly different in the FM and SDW phases. The derived magnetic moments for the FM and SDW phases from the neutron diffraction experiments are in good agreement with the values [43] obtained by density functional theory calculations for the FM and AFM phases, respectively.

In order to explore the phase transition in detail for S1, we further analyzed the Bragg peak at $Q \approx 0.42$ Å^{-1} [see Fig. 3(b)], which is indexed to be the (0.355 0 0) magnetic reflection of the SDW phase. Above 60 K, the Bragg peak transforms into diffuse scattering, suggesting

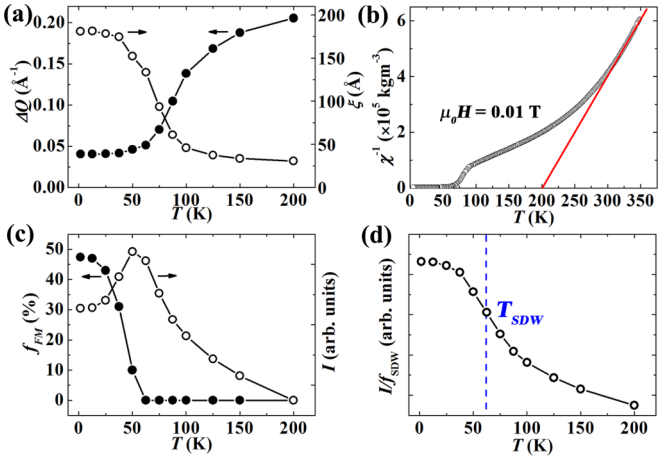

FIG. 5. (a) Peak width of the (0.355 0 0) magnetic reflection. (b) Temperature-dependent inverse susceptibility. (c) Weight fraction of the FM phase and integrated intensity of the (0.355 0 0) magnetic reflection at different temperatures. (d) Temperature dependence of the normalized intensity of the (0.355 0 0) magnetic reflection.

the presence of short-range magnetic correlations [44]. The thermal evolution of the full-width-at-half-maximum (ΔQ) of the (0.355 0 0) peak is presented in Fig. 5(a). The correlation length $\xi = 2\pi/\Delta Q$ is estimated to be 30 Å at 200 K, and increases with decreasing temperature to about 180 Å in the magnetically ordered state [see Fig. 5(a)]. The presence of short-range magnetic ordering above 60 K is also suggested by the bulk susceptibility measurement [see Fig. 5(b)], where the inverse susceptibility shows a strong deviation from the Curie-Weiss behavior below 300 K. The integrated intensity of the (0.355 0 0) peak as a function of temperature is presented in Fig. 5(c). The integrated intensity rises with decreasing temperature from 200 to 50 K, which is attributed to the weakening of the magnetic fluctuations. The reduction in the integrated intensity below 50 K is due to the decreasing fraction of the SDW phase caused by the SDW to FM phase transition. Structure refinement reveals that there is no detectable FM phase above 62.5 K, and f_{FM} increases from about 10% at 50 K to around 47% at 1.5 K upon cooling. In order to exclude the influence of the SDW-FM transition on the integrated intensity of the (0.355 0 0) peak, the integrated intensity in Fig. 5(c) is normalized by the phase fraction of the SDW phase. The normalized intensity is presented in Fig. 5(d). Since the normalized intensity is proportional to M^2, a critical temperature T_{SDW} of about 62.5 K for the PM-SDW transition can be derived by taking the maximum in the derivative of the normalized intensity with respect to temperature.

The lattice parameters extracted from the refinement at different temperatures are shown in Fig. 6. The anomalous thermal expansion in the lattice parameters between 200 and 62.5 K is associated with the development of short-range magnetic correlations. The lattice parameters show a continuous change around the PM-SDW transition temperature ($T_{\mathrm{SDW}} \approx 62.5$ K), implying a second-order phase transition. The jump in lattice parameters, which accompanies the SDW-FM transition ($T_C \approx 50$ K), characterizes the first-order nature of the transition and the strong magnetoelastic coupling.

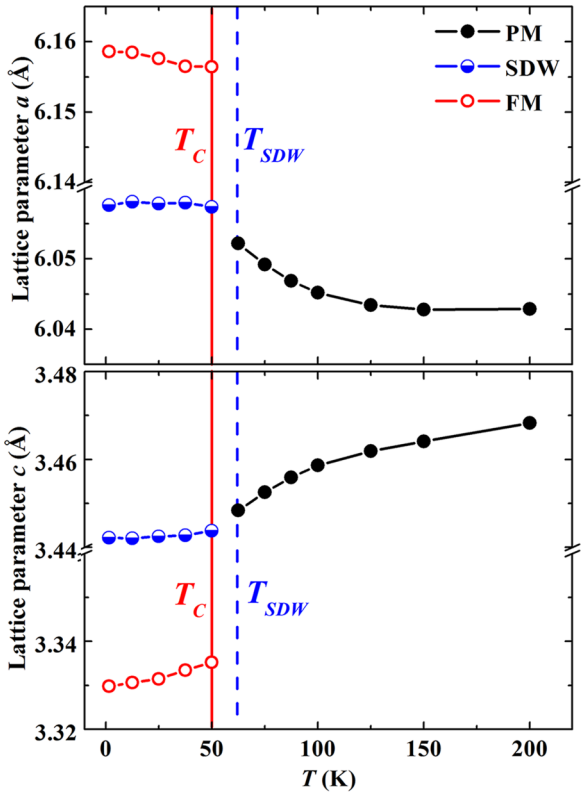

FIG. 6. Lattice parameters as a function of temperature derived from neutron diffraction for S1.

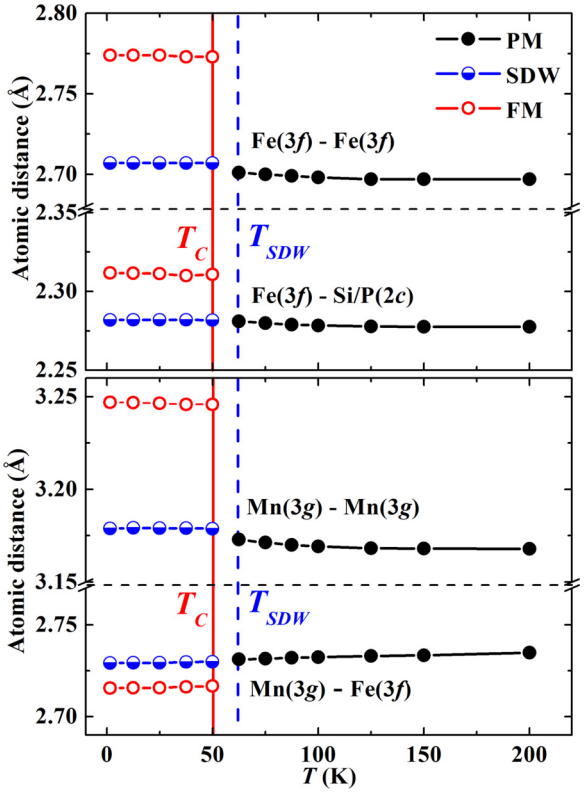

FIG. 7. Thermal evolution of interatomic distances extracted from neutron diffraction for S1.

The changes in lattice parameter correspond to variations in the interatomic distances, which are coupled with the magnetic exchange interactions. The $(Mn,Fe)_2(P,Si)$ compound crystallizes in a hexagonal structure. The Fe and Mn atoms prefer to occupy the $3f$ and $3g$ sites, respectively, which are on different atomic layers along the c axis of the hexagonal structure. The Si and P atoms occupy the $2c$ and $1b$ sites, which are on the same atomic layer as the $3f$ and $3g$ sites, respectively. As shown in Fig. 7, the intralayer atomic distances gradually increase with the decrease in temperature until the SDW-FM transition temperature is reached, where a jump in the interatomic distances occurs. The Fe-Mn interlayer atomic distance experiences a drop at the SDW-FM transition temperature. A significant expansion in the intralayer bonds after the SDW-FM transition leads to a stronger localization of Fe and Mn $3d$ electrons and less chemical bonding with neighboring atoms in the FM phase. Also, the smaller distance between Mn and Fe atoms in the FM phase enhances the magnetic exchange interaction between them. As a result, a ferromagnetic coupling is more favorable at low temperatures.

C. Mössbauer measurements

^{57}Fe Mössbauer spectroscopy allows us to further investigate the magnetic ordering of the Fe atoms in the SDW and FM phases. Mössbauer spectra of the as-prepared S0–S3, measured at 300 K are presented in Figs. 8(a)–8(d), respectively. All spectra exhibit a paramagnetic feature. According to the neutron diffraction results (see Table I), the P and Si atoms are randomly distributed in the tetrahedral environment around Fe atoms in the studied samples. As a result, there are five different nearest-neighbor Fe configurations, depending on the number (from 0 to 4) of Si atoms in the tetrahedral environment. Their contributions to the Mössbauer spectrum can be described by a binomial distribution model, which has been successfully used for Mössbauer analysis in $(Mn,Fe)_2(P,Si)$-type compounds [45,46]. The same fitting approach was adopted for the present study. The nominal Si/P ratios were used in

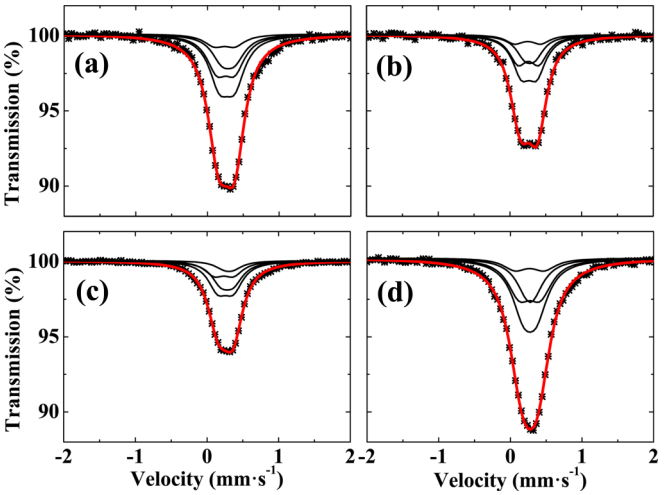

FIG. 8. Mössbauer spectra collected at 300 K for the as-prepared S0 (a), S1 (b), S2 (c), and S3 (d). The black and red solid lines are individual binomial PM components and their sum, respectively.

TABLE II. Hyperfine parameters at 300 K for the as-prepared S0–S3.

Sample	$\langle\delta\rangle$[a] (mm/s)	$\langle\varepsilon\rangle$ (mm/s)	Γ (mm/s)
S0	0.27(1)	0.22(1)	0.34(1)
S1	0.26(1)	0.24(1)	0.30(1)
S2	0.26(1)	0.21(1)	0.32(1)
S3	0.27(1)	0.22(1)	0.39(1)

[a]The isomer shifts reported hereafter are given relative to α-iron at 300 K.

the binomial distribution model for all samples. Hyperfine parameters obtained from the fitting are presented in Table II. The average isomer shift $\langle\delta\rangle$, average quadrupole splitting $\langle\varepsilon\rangle$, and linewidth Γ are in good agreement with previous reports in $(Mn,Fe)_2(P,Si)$-type compounds [45–47].

Figure 9(a) shows the Mössbauer spectrum measured at 4.2 K for S0 after zero-field cooling. The observed sextet with broad spectral lines suggests a strong magnetic ordering with a distribution of hyperfine fields around the Fe nucleus, which can be fitted with a binomial distribution model [46]. In contrast, the 4.2 K Mössbauer spectra of S1–S3 display a complicated shape, as shown in Figs. 9(b)–9(d). As revealed by the neutron diffraction results, S1 is a mixture of FM and SDW phases below 50 K. As a result, the 4.2 K Mössbauer spectra of S1–S3 can be decomposed into FM and incommensurate magnetic components. The FM component was fitted with the binomial distribution model [46], and the incommensurate magnetic component was fitted with a field-distribution model that takes into account the sinusoidally modulated Fe moment. For the incommensurate-magnetic component, the hyperfine field H_{SDW} experienced by an Fe nucleus can be described as

$$H_{SDW} = H^m_{SDW} \sin\theta, \quad (1)$$

where H^m_{SDW} is the magnitude of the hyperfine field, which is modulated by a sine function. The sign of the hyperfine field has no influence on the spectrum. As a result, the incommensurate-magnetic contribution can be obtained by integration over $0 \leqslant \theta \leqslant \pi/2$ for Eq. (1). The above model gives a reasonable fit to the 4.2 K Mössbauer spectra for S1–S3.

The derived hyperfine parameters are presented in Table III. It should be noted that the incremental hyperfine parameters (see Table III) used in the binomial distribution model, i.e., the incremental isomer shift ($\Delta\delta$), quadrupole splitting ($\Delta\varepsilon$), and hyperfine field (ΔH), were constrained to be equal for the 4.2

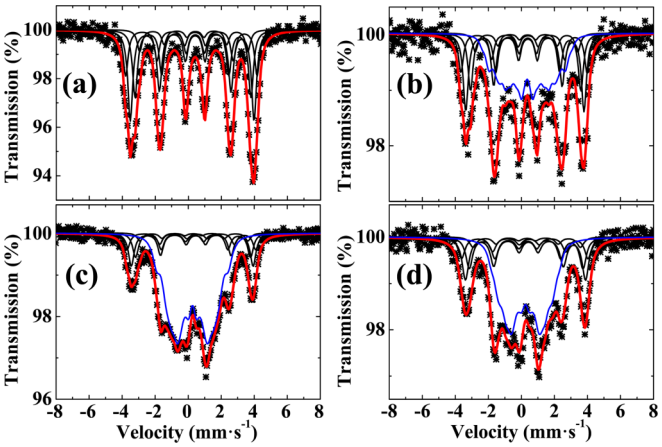

FIG. 9. Mössbauer spectra obtained at 4.2 K for the as-prepared S0 (a), S1 (b), S2 (c), and S3 (d). The black, blue, and red lines are individual binomial FM components, the SDW component, and their sum, respectively.

and 300 K Mössbauer spectra. The Mössbauer experiments suggest that S0 is a pure FM phase at 4.2 K. For S1, the f_{FM} derived from Mössbauer spectrum is about 61(3)%, which is higher than the value of 47.4(2)% derived from neutron diffraction measurements in Table I. A smaller fraction of FM phase is present at 4.2 K in S2 and S3 than in S1, which is consistent with the magnetization results (see Figs. 1 and 2). The derived average quadrupole splitting and hyperfine field at 4.2 K for the FM phase is in good agreement with those reported for the isostructural $(Mn,Fe)_2(P,Ge)$ compounds [48]. However, the $(Mn,Fe)_2(P,Si)$ compounds show smaller average isomer shifts than the $(Mn,Fe)_2(P,Ge)$ compounds, which is probably due to the smaller unit-cell volumes for the $(Mn,Fe)_2(P,Si)$ compounds. We observed a clear difference in the isomer shift between the 300 and 4.2 K measurements, although the source and the samples were always at the same temperature. This difference reflects the changes in the chemical environment around the Fe atoms during the magnetoelastic transition. Our recent studies [43] reveal that there is a significant redistribution of electronic density around the Fe atoms during the magnetoelastic transition. Also, a significant difference in the lattice parameters (see Fig. 6) is observed between 4.2 and 300 K. These two factors cause the observed difference in the isomer shift between the 300 and 4.2 K measurements. Additionally, the linewidth for S3 is

TABLE III. Hyperfine parameters at 4.2 K for the as-prepared S0–S3.

Sample	$\langle\delta\rangle$ (mm/s)	$\langle\varepsilon\rangle$ (mm/s)	Γ (mm/s)	$\mu_0 H$ (T)	$\Delta\delta$ (mm/s)	$\Delta\varepsilon$ (mm/s)	ΔH (%)	Phase	Fraction (%)
S0	0.33(1)	−0.17(1)	0.36(1)	22.8(1)	0.01	0.04	1.5	FM	100
S1	0.31(1)	−0.17(1)	0.37(1)	21.8(1)	0.01	0.06	1.5	FM	61(3)
	0.35(1)	–	0.37(1)	17.7(5)	–	–	–	SDW	39(3)
S2	0.35(1)	−0.17(1)	0.42(1)	22.7(1)	0.01	0.06	1.5	FM	35(3)
	0.36(1)	–	0.42(1)	18.8(5)	–	–	–	SDW	65(3)
S3	0.34(1)	−0.16(1)	0.49(1)	22.2(1)	0.01	0.05	1.5	FM	41(3)
	0.35(1)	–	0.50(1)	18.4(5)	–	–	–	SDW	59(3)

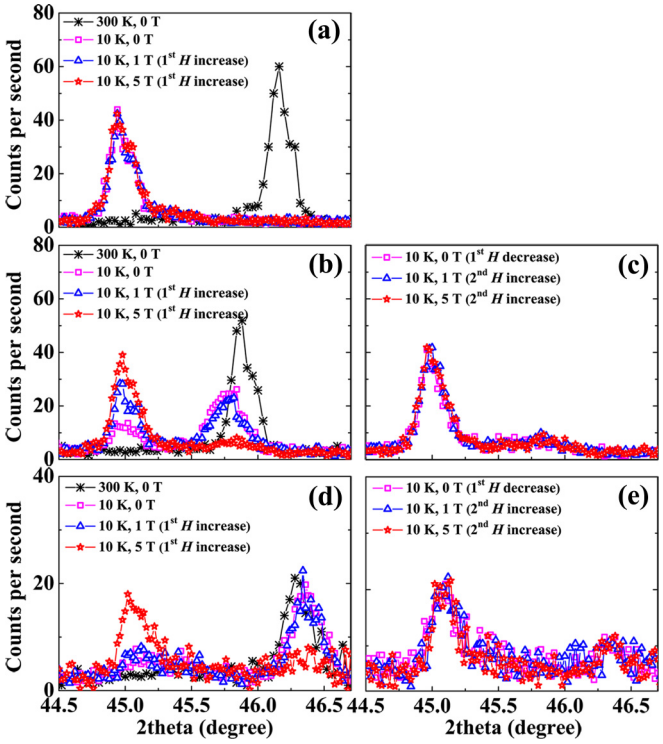

FIG. 10. XRD patterns measured at 300 and 10 K in different magnetic field for the as-prepared S0 (a), S1 (b) and (c), and S3 (d) and (e).

significantly larger than that for other samples. This is due to the influence of the N doping on the chemical environment around the Fe atoms. Our recent studies [49] show that N dopants occupy both the substitutional $1b$ site and the interstitial $6j$ and $6k$ sites in the crystal structure. This leads to a larger variation in nearest-neighbor Fe configurations in S3, which causes a larger linewidth for the Mössbauer spectrum.

For S1, the magnitude of the hyperfine fields is about 21.8 and 17.7 T for the FM and SDW phases at 4.2 K, respectively. Using a proportionality factor of 14.2 T/μ_B, as proposed by Eriksson and Svane [50], the Fe moments in the FM and SDW phases are estimated to be 1.5 and 1.2 μ_B, which is in reasonable agreement with the neutron diffraction results in Table I. Consequently, the SDW to FM transition is accompanied by a significant increase in the Fe moment and a slight change in the Mn moment, which characterizes the unique mixed magnetism in the $(Mn,Fe)_2(P,Si)$-type compounds. The Fe atoms on the $3f$ site show a low moment to high moment transition. The development of the Fe moment is in strong competition with the formation of chemical bonds, which in turn depends on the interatomic distances between Fe and its neighbors (shown in Fig. 7). The size of the Mn moment on the $3g$ site is less influenced by the interatomic distances, which reflects the localized character of the Mn moment.

D. In-field x-ray diffraction

X-ray powder diffraction was measured at 300 and 10 K for the as-prepared S0, S1, and S3. Structure refinement confirms the hexagonal Fe_2P-type structure ($P\bar{6}2m$) at the two temperatures for all three samples. When the as-prepared S0 is cooled down from 300 to 10 K, a significant shift in the (210) Bragg peak appears in the XRD pattern [see Fig. 10(a)], indicating a strong magnetoelastic coupling. In the x-ray diffraction pattern, there is no detectable phase coexistence in S0 at 10 K. This is in agreement with the Mössbauer results shown in Table III. XRD patterns were then collected for different magnetic fields at a constant temperature of 10 K [see Fig. 10(a)]. The applied magnetic field has little influence on the XRD patterns.

TABLE IV. Structural parameters for S0, S1, and S3 in different magnetic states obtained from x-ray diffraction.

Parameter	Phase	S0	S1	S3
a (Å)	PM	6.013(1)	6.055(1)	6.014(1)
	SDW	–	6.058(1)	6.009(2)
	FM	6.157(1)	6.158(1)	6.142(2)
c (Å)	PM	3.478(1)	3.474(1)	3.484(1)
	SDW	–	3.442(1)	3.474(2)
	FM	3.299(1)	3.331(1)	3.305(2)
c/a	PM	0.578(1)	0.574(1)	0.579(1)
	SDW	–	0.568(1)	0.578(2)
	FM	0.536(1)	0.541(1)	0.538(2)

The XRD pattern of S1 collected at 10 K after zero-field cooling is in strong contrast to that of S0. Two Bragg peaks appear at 2θ values of 45.0° and 45.8°, respectively. Structure refinement reveals that these two peaks belong to the (210) Bragg peak of two phases having the same crystal structure but with different lattice parameters. For increasing magnetic fields, the peak at $2\theta \approx 45.0°$ grows at the expense of the peak at ≈45.8° [Fig. 10(b)], which clearly demonstrates the field-induced metamagnetic SDW-FM transition. At 5 T, the peak at $2\theta \approx 45.8°$ has almost disappeared. After the XRD measurement in 5 T, the magnetic field was removed and an XRD pattern was collected in 0 T. No change in the XRD pattern is observed after the removal of the magnetic field, nor during the subsequent field-increasing process. This is evidence of the irreversibility of the SDW to FM transition, which is also observed in our magnetization measurements in Fig. 1(d).

The coexistence of the SDW and FM phases is also observed in the XRD pattern [Fig. 10(d)] of S3 measured at 10 K after zero-field cooling. The field-induced SDW-FM transition is manifested by the increasing intensity of the FM (210) peak at ≈45.1° with increasing magnetic field. The SDW-FM transition is still not complete at 5 T, as indicated by the remaining peak at $2\theta \approx 46.3°$. There is no signature of a recovery of the SDW phase during the subsequent field cycle at 10 K [see Fig. 10(e)].

The structural parameters derived from Rietveld refinement for S0, S1, and S3 are summarized in Table IV. The magnetic transition is strongly coupled to variations in the lattice parameters. The FM configuration is in competition with an incommensurate magnetic configuration in the $(Mn,Fe)_2(P,Si)$ compounds, and the relative stability of the two configurations strongly depends on the c/a ratio [29]. The stability of the incommensurate magnetic configuration is enhanced with the increase in c/a ratio [29]. As a result, a metastable

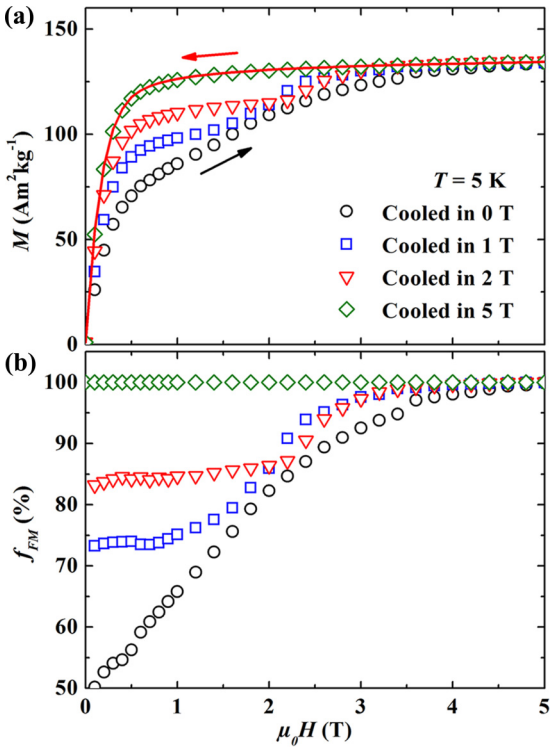

FIG. 11. (a) Isothermal M-H curves for the as-prepared S1 cooled in different magnetic fields. Open symbols indicate the magnetization process, and the solid line shows the demagnetization process. The demagnetization curve is the same for all four conditions. (b) Derived f_{FM}-H at 5 K after cooling in different magnetic fields.

incommensurate magnetic configuration forms in S1 and S3 with large c/a ratios at low temperature. Additionally, S1 and S3 have a low T_C, as indicated by the magnetization results shown in Figs. 1 and 2. Due to the small thermal energy at low temperatures, the phase transition from the metastable incommensurate phase to stable FM phase may be kinetically arrested. As a consequence, the metastable incommensurate SDW phase coexists with the stable FM phase at low temperatures in S1 and S3. An external magnetic field promotes the FM phase and therefore drives the SDW to FM transition.

E. Metastability of the SDW phase

For further study on the metastability of the SDW phase, we used S1 since its SDW-FM transition can be triggered by field and completed below 5 T at low temperatures [see Fig. 1(d)]. Figure 11(a) compares isothermal M-H curves measured at 5 K after cooling in different magnetic fields. To avoid any thermal- or field-history effects, each M-H measurement was performed on a different piece of the sample from the same batch. A field-induced SDW-FM transition is present in all the samples cooled in a magnetic field below 5 T. No metamagnetic transition appears in the subsequent decrease and increase in magnetic field, indicating the formation of a stable FM phase. Since the SDW phase has no net magnetization, the measured magnetization is proportional to the fraction of FM phase (f_{FM}). If we assume that the sample cooled in 5 T is a pure FM phase (i.e., $f_{\mathrm{FM}} = 100\%$), then the f_{FM}-H curve at 5 K for samples cooled in different fields can be derived using $M(H)/M_{5\,\mathrm{T}}(H)$. Figure 11(b) shows that the sample cooled in zero magnetic field contains about 50(2)% FM phase at 5 K, which is in good agreement with the $f_{\mathrm{FM}} = 47.4(2)\%$ obtained from the neutron diffraction experiments. The higher f_{FM} value of 61(3)% derived from the Mössbauer spectrum is expected to be due to the oversimplified model used for fitting the SDW component in the Mössbauer spectrum. The FM fraction increases rapidly with increasing H, reaching 100% at about 4 T. For the samples cooled in 1 and 2 T, the f_{FM} remains nearly constant when the applied magnetic field is lower than the cooling field, as illustrated by the initial plateau in the f_{FM}-H curves. When the applied magnetic field exceeds the cooling field, the SDW-FM transition is triggered and completed at around 4 T. It should be noted that there is a clear difference in the f_{FM} at $\mu_0 H = 1$ T between the samples cooled in 0 and 1 T [see Fig. 11(b)]. This difference is due to the kinetic nature of the SDW-FM transition.

A special magnetic measurement protocol, i.e., cooling and heating in unequal fields ("CHUF") proposed by Banerjee *et al.* [24,40], provides a method to identify the kinetic-arrest-induced phase coexistence and its metastability. After cooling from 300 to 5 K in 0, 1, and 5 T, respectively, a magnetic field of 1 T was applied and M-T measurements were performed on warming. The M-T curve of the sample cooled in zero field shows an initial increase below 20 K and then merges with the M-T curve of the sample cooled in 1 T [see Fig. 12(a)]. The initial increase of the magnetization with increasing temperature is associated with the de-arrest of the SDW-FM transition and the resulting increase of the FM fraction. The SDW phase is highly metastable and the increasing T and H converts it to the stable FM phase. A high magnetization is observed for the sample cooled in 5 T due to the absence of the SDW phase, as suggested in Fig. 11(b).

Magnetization relaxation measurements at various temperatures provide further evidence for the metastability of the SDW phase. The as-prepared S1 was cooled down to various measurement temperatures in zero magnetic field. After that, a magnetic field of 1 T was applied and the magnetization was measured immediately after the field stabilization. As depicted in Fig. 12(b), a notable relaxation in M highlights the metastability of the SDW phase. With the decrease in temperature, the relaxation becomes less pronounced. The Kohlrausch-Williams-Watt stretched exponential function [51,52] $\Phi(t) \propto \exp[-(t/\tau)^{\beta}]$ has been widely used to describe the magnetic relaxation behavior in kinetically arrested systems [13,16,17], where τ is the characteristic relaxation time and β is a shape parameter. The relaxation data below 20 K can be fit well using the stretched exponential function with $\beta = 0.18$, while noticeable deviations appear above 20 K. The τ increases markedly with decreasing temperature due to the reduction in thermal fluctuation, as shown in the inset of Fig. 12(b). An activation energy of $\Delta E = 0.24(3)$ kJ/mol can be derived for S1 from the $\ln(\tau)$-T curve based on the Arrhenius equation. The derived activation energies for S2 and S3 are 0.32(5) and 0.36(6), respectively. The calculated activation energy corresponds to the energy barrier for the nucleation of the ferromagnetic phase. The large changes in lattice parameters during the SDW-FM transition (see Fig. 6) will result in

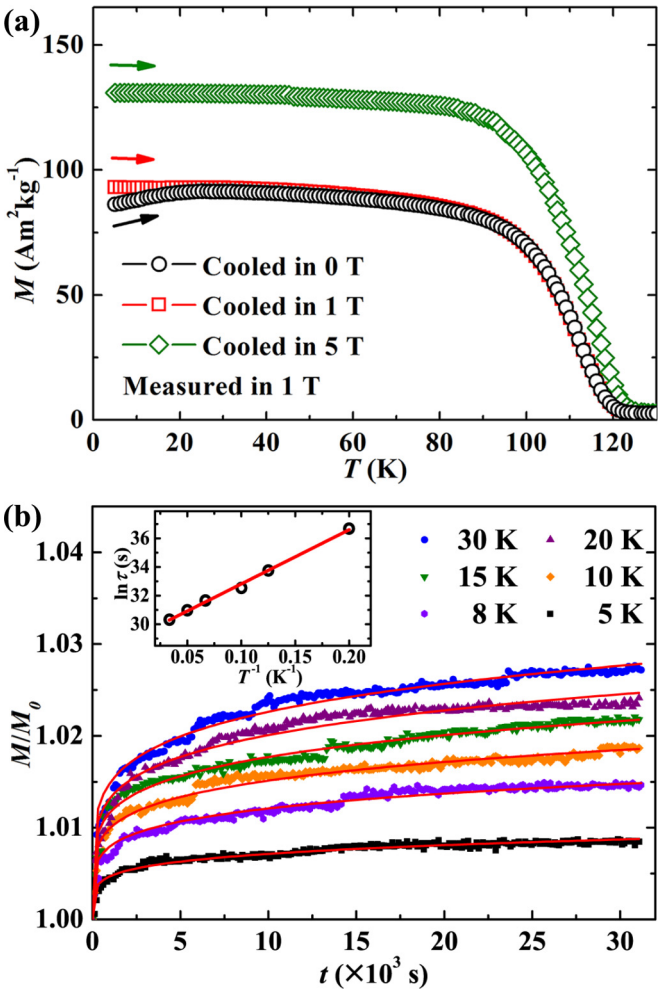

FIG. 12. (a) Temperature-dependent magnetization of S1 measured during warming after being cooled in different magnetic fields. (b) Magnetization versus time measured at 5 K after zero-field cooling. The temperature dependence of the characteristic relaxation time is shown in the inset.

a sizable elastic shear strain at the interface between the SDW and FM phases. The corresponding elastic energy will contribute significantly to the energy barrier for nucleation of the ferromagnetic phase.

IV. CONCLUSIONS

In contrast to the common PM-FM phase transition in $(Mn,Fe)_2(P,Si)$ compounds, a PM-SDW-FM transition is observed for the $Mn_{1.30}Fe_{0.65}P_{0.67}Si_{0.33}$, $MnFe_{0.95}P_{0.71}Si_{0.29}$, and $MnFe_{0.95}P_{0.67}Si_{0.33}N_{0.02}$ compositions. The PM-SDW transition is of second order and accompanied with continuous changes in the lattice parameters. The SDW-FM transition, first order in nature, is strongly coupled to discontinuous variations in the lattice parameters. The SDW-FM transition can be kinetically arrested, leading to a coexistence of the FM phase and the untransformed SDW phase at low temperature. The untransformed SDW phase is metastable at low temperatures, and can be converted to the stable FM phase by applying a magnetic field. The formation of the SDW phase originates from the lower stability of the FM phase at large *c*/*a* ratios. The SDW-FM transition is accompanied by a significant increase in the Fe moment and a slight change in the Mn moment. This study sheds new light on the strong magnetoelastic coupling and mixed magnetism in the $(Mn,Fe)_2(P,Si)$ system.

ACKNOWLEDGMENTS

The authors thank Anton Lefering and Bert Zwart for their help with the sample preparation. This work is part of the Industrial Partnership Program of the Dutch Foundation for Fundamental Research on Matter (FOM), and co-financed by BASF New Business.

APPENDIX: DETERMINATION OF THE MAGNETIC STRUCTURE OF THE SDW PHASE

Determination of magnetic structures using neutron powder diffraction usually follows four steps: (i) extract the magnetic

TABLE V. Structural details derived from Rietveld refinement using different magnetic configurations for the $Mn_{1.30}Fe_{0.65}P_{0.67}Si_{0.33}$ (S1) sample.

Angle between Fe and Mn moments	Moment directions	Fe moment (μ_B)	Mn moment (μ_B)	R_{Mag} factor (%)
0°	$\boldsymbol{M}_{Fe} \parallel \boldsymbol{c}$, $\boldsymbol{M}_{Mn} \parallel \boldsymbol{c}$	0.3(5)	1.6(5)	44.4
	$\boldsymbol{M}_{Fe} \parallel \boldsymbol{a}^*$, $\boldsymbol{M}_{Mn} \parallel \boldsymbol{a}^*$	0.7(3)	2.3(3)	24.1
	$\boldsymbol{M}_{Fe} \parallel \boldsymbol{b}$, $\boldsymbol{M}_{Mn} \parallel \boldsymbol{b}$	0.1(4)	3.2(4)	32.9
30°	$\boldsymbol{M}_{Fe} \parallel \boldsymbol{a}$, $\boldsymbol{M}_{Mn} \parallel \boldsymbol{a}^*$	0.7(2)	2.9(2)	11.9
	$\boldsymbol{M}_{Fe} \parallel \boldsymbol{a}^*$, $\boldsymbol{M}_{Mn} \parallel \boldsymbol{a}$	0.5(2)	3.0(2)	12.9
	$\boldsymbol{M}_{Fe} \parallel \boldsymbol{b}$, $\boldsymbol{M}_{Mn} \parallel \boldsymbol{b}^*$	0.5(3)	2.9(3)	24.8
	$\boldsymbol{M}_{Fe} \parallel \boldsymbol{b}^*$, $\boldsymbol{M}_{Mn} \parallel \boldsymbol{b}$	0.8(4)	1.8(4)	37.2
60°	$\boldsymbol{M}_{Fe} \parallel \boldsymbol{b}^*$, $\boldsymbol{M}_{Mn} \parallel \boldsymbol{a}^*$	0.8(2)	3.0(2)	12.9
	$\boldsymbol{M}_{Fe} \parallel \boldsymbol{a}^*$, $\boldsymbol{M}_{Mn} \parallel \boldsymbol{b}^*$	2.6(3)	1.9(3)	19.8
90°	$\boldsymbol{M}_{Fe} \parallel \boldsymbol{b}$, $\boldsymbol{M}_{Mn} \parallel \boldsymbol{a}^*$	0.8(2)	3.1(2)	8.4
	$\boldsymbol{M}_{Fe} \parallel \boldsymbol{a}^*$, $\boldsymbol{M}_{Mn} \parallel \boldsymbol{b}$	2.6(3)	0.7(3)	18.6
120°	$\boldsymbol{M}_{Fe} \parallel \boldsymbol{b}$, $\boldsymbol{M}_{Mn} \parallel \boldsymbol{a}$	0.2(3)	3.1(3)	17.2
	$\boldsymbol{M}_{Fe} \parallel \boldsymbol{a}$, $\boldsymbol{M}_{Mn} \parallel \boldsymbol{b}$	2.3(4)	1.2(4)	31.7

reflections from the diffraction patterns; (ii) obtain the propagation vector $\boldsymbol{k}$ of the unknown magnetic structure based on the positions of the magnetic reflections; (iii) perform representation analysis to get irreducible representations (IRs); and (iv) according to IRs, try different magnetic configurations to find out the reasonable and best solutions.

As discussed in the main text, the satellite reflections and the peak at $Q \approx 0.42\,\text{Å}^{-1}$ are the contributions from the unknown magnetic phase. We performed an automatic $\boldsymbol{k}$-indexing procedure using the $\boldsymbol{k}$-search program in the Fullprof package [34]. A propagation vector of $\boldsymbol{k} = (0.355(1),0,0)$ is obtained, which is along the primitive vector $\boldsymbol{a}^*$ in the reciprocal space. This indicates an incommensurate magnetic structure (i.e., a helical spin configuration or a spin-density wave), propagating along the $\boldsymbol{a}^*$ in the reciprocal space.

The representation analysis [41,42] was performed using the BasIreps program in the Fullprof package [34]. Representation analysis yields two nonzero irreducible representations (IRs) for both Fe and Mn moments on the $3f$ and $3g$ sites, respectively. One IR corresponds to both Fe and Mn moments along the c axis, and the other corresponds to both moments within the ab plane. A helical spin configuration with $\boldsymbol{k} = (0.355,0,0)$ is not allowed by the IRs. As a result, the incommensurate-magnetic phase can be described by a sinusoidal spin-density wave (SDW) with $\boldsymbol{k} = (0.355,0,0)$.

We tried to fit the diffraction patterns using different magnetic configurations, as shown in Table V. The spin density wave with the Mn and Fe moments parallel and perpendicular to $\boldsymbol{k}$, respectively, gives the best fit with a magnetic R factor of about 8.4%. A schematic representation of the magnetic structure is shown in Fig. 4.

[1] V. K. Pecharsky and K. A. Gschneidner, Jr., Phys. Rev. Lett. **78**, 4494 (1997).

[2] O. Tegus, E. Brück, K. H. J. Buschow, and F. R. de Boer, Nature (London) **415**, 150 (2002).

[3] A. Fujita, S. Fujieda, Y. Hasegawa, and K. Fukamichi, Phys. Rev. B **67**, 104416 (2003).

[4] R. von Helmolt, J. Wecker, B. Holzapfel, L. Schultz, and K. Samwer, Phys. Rev. Lett. **71**, 2331 (1993).

[5] S. Jin, T. H. Tiefel, M. McCormack, R. A. Fastnacht, R. Ramesh, and L. H. Chen, Science **264**, 413 (1994).

[6] K. Ullakko, J. K. Huang, C. Kantner, R. C. OHandley, and V. V. Kokorin, Appl. Phys. Lett. **69**, 1966 (1996).

[7] S. J. Park, H. W. Yeom, J. R. Ahn, and I. W. Lyo, Phys. Rev. Lett. **95**, 126102 (2005).

[8] S. B. Roy, G. K. Perkins, M. K. Chattopadhyay, A. K. Nigam, K. J. S. Sokhey, P. Chaddah, A. D. Caplin, and L. F. Cohen, Phys. Rev. Lett. **92**, 147203 (2004).

[9] D. D. Sarma, D. Topwal, U. Manju, S. R. Krishnakumar, M. Bertolo, S. La Rosa, G. Cautero, T. Y. Koo, P. A. Sharma, S.-W. Cheong, and A. Fujimori, Phys. Rev. Lett. **93**, 097202 (2004).

[10] A. Soibel, E. Zeldov, M. Rappaport, Y. Myasoedov, T. Tamegai, S. Ooi, M. Konczykowski, and V. B. Geshkenbein, Nature (London) **406**, 282 (2000).

[11] M. E. Brown, A. H. Bouchez, and C. A. Griffith, Nature (London) **420**, 795 (2002).

[12] W. Wu, C. Israel, N. Hur, S. Park, S. W. Cheong, and A. de Lozanne, Nat. Mater. **5**, 881 (2006).

[13] M. K. Chattopadhyay, S. B. Roy, and P. Chaddah, Phys. Rev. B **72**, 180401 (2005).

[14] M. A. Manekar, S. Chaudhary, M. K. Chattopadhyay, K. J. Singh, S. B. Roy, and P. Chaddah, Phys. Rev. B **64**, 104416 (2001).

[15] S. B. Roy, P. Chaddah, V. K. Pecharsky, and K. A. Gschneidner, Acta Mater. **56**, 5895 (2008).

[16] S. B. Roy, M. K. Chattopadhyay, P. Chaddah, J. D. Moore, G. K. Perkins, L. F. Cohen, K. A. Gschneidner, and V. K. Pecharsky, Phys. Rev. B **74**, 012403 (2006).

[17] V. K. Sharma, M. K. Chattopadhyay, and S. B. Roy, Phys. Rev. B **76**, 140401 (2007).

[18] R. Y. Umetsu, K. Ito, W. Ito, K. Koyama, T. Kanomata, K. Ishida, and R. Kainuma, J. Alloys Compd. **509**, 1389 (2011).

[19] W. Ito, K. Ito, R. Y. Umetsu, R. Kainuma, K. Koyama, K. Watanabe, A. Fujita, K. Oikawa, K. Ishida, and T. Kanomata, Appl. Phys. Lett. **92**, 021908 (2008).

[20] P. Kushwaha, A. Lakhani, R. Rawat, and P. Chaddah, Phys. Rev. B **80**, 174413 (2009).

[21] K. Sengupta and E. V. Sampathkumaran, Phys. Rev. B **73**, 020406 (2006).

[22] K. Mukherjee, S. D. Das, N. Mohapatra, K. K. Iyer, and E. V. Sampathkumaran, Phys. Rev. B **81**, 184434 (2010).

[23] H. Kuwahara, Y. Tomioka, A. Asamitsu, Y. Moritomo, and Y. Tokura, Science **270**, 961 (1995).

[24] A. Banerjee, A. K. Pramanik, K. Kumar, and P. Chaddah, J. Phys.: Condens. Matter **18**, L605 (2006).

[25] K. Kumar, A. K. Pramanik, A. Banerjee, P. Chaddah, S. B. Roy, S. Park, C. L. Zhang, and S. W. Cheong, Phys. Rev. B **73**, 184435 (2006).

[26] R. Rawat, K. Mukherjee, K. Kumar, A. Banerjee, and P. Chaddah, J. Phys.: Condens. Matter **19**, 256211 (2007).

[27] A. Shahee, D. Kumar, C. Shekhar, and N. P. Lalla, J. Phys.: Condens. Matter **24**, 225405 (2012).

[28] V. Höglin, M. Hudl, L. Caron, P. Beran, M. H. Sorby, P. Nordblad, Y. Andersson, and M. Sahlberg, J. Solid State Chem. **221**, 240 (2015).

[29] E. K. Delczeg-Czirjak, M. Pereiro, L. Bergqvist, Y. O. Kvashnin, I. Di Marco, G. Li, L. Vitos, and O. Eriksson, Phys. Rev. B **90**, 214436 (2014).

[30] G. Li, W. Li, S. Schönecker, X. Li, E. K. Delczeg-Czirjak, Y. O. Kvashnin, O. Eriksson, B. Johansson, and L. Vitos, Appl. Phys. Lett. **105**, 262405 (2014).

[31] N. H. Dung, L. Zhang, Z. Q. Ou, L. Zhao, L. van Eijck, A. M. Mulders, M. Avdeev, E. Suard, N. H. van Dijk, and E. Brück, Phys. Rev. B **86**, 045134 (2012).

[32] L. C. Chapon, P. Manuel, P. G. Radaelli, C. Benson, L. Perrott, S. Ansell, N. J. Rhodes, D. Raspino, D. Duxbury, E. Spill, and J. Norris, Neutron News **22**, 22 (2011).

[33] K. Watanabe, Y. Watanabe, S. Awaji, M. Fujiwara, N. Kobayashi, and T. Hasebe, in *Advances in Cryogenic Engineering Materials*, edited by U. B. Balachandran, D. G. Gubser, K. T. Hartwig, R. P. Reed, W. H. Warnes, and V. A. Bardos, Vol. 44 (Springer, New York, 1998), pp. 747–752.

[34] J. Rodríguez-Carvajal, Physica B **192**, 55 (1993).

[35] J. V. Leitão, X. M. You, L. Caron, and E. Brück, J. Alloys Compd. **520**, 52 (2012).
[36] Z. Klencsár, Nucl. Instrum. Methods Phys. Res., Sect. B **129**, 527 (1997).
[37] X. F. Miao, L. Caron, Z. Gercsi, A. Daoud-Aladine, N. H. van Dijk, and E. Brück, Appl. Phys. Lett. **107**, 042403 (2015).
[38] F. Guillou, G. Porcari, H. Yibole, N. H. van Dijk, and E. Brück, Adv. Mater. **26**, 2671 (2014).
[39] N. H. Dung, L. Zhang, Z. Q. Ou, and E. Brück, Appl. Phys. Lett. **99**, 092511 (2011).
[40] A. Banerjee, K. Kumar, and P. Chaddah, J. Phys.: Condens. Matter **21**, 026002 (2009).
[41] E. F. Bertaut, Acta Crystallogr. Sect. A **24**, 217 (1968).
[42] E. F. Bertaut, J. Magn. Magn. Mater. **24**, 267 (1981).
[43] M. F. J. Boeije, P. Roy, F. Guillou, H. Yibole, X. F. Miao, L. Caron, D. Banerjee, N. H. van Dijk, R. A. de Groot, and E. Brück, Chem. Mater. **28**, 4901 (2016).
[44] X. F. Miao, L. Caron, J. Cedervall, P. C. M. Gubbens, P. Dalmas de Réotier, A. Yaouanc, F. Qian, A. R. Wildes, H. Luetkens, A. Amato, N. H. van Dijk, and E. Brück, Phys. Rev. B **94**, 014426 (2016).
[45] B. Malaman, G. L. Caer, P. Delcroix, D. Fruchart, M. Bacmann, and R. Fruchart, J. Phys.: Condens. Matter **8**, 8653 (1996).
[46] R. P. Hermann, O. Tegus, E. Brück, K. H. J. Buschow, F. R. de Boer, G. J. Long, and F. Grandjean, Phys. Rev. B **70**, 214425 (2004).
[47] M. Hudl, P. Nordblad, T. Björkman, O. Eriksson, L. Häggström, M. Sahlberg, Y. Andersson, E. K. Delczeg-Czirjak, and L. Vitos, Phys. Rev. B **83**, 134420 (2011).
[48] M. T. Sougrati, R. P. Hermann, F. Grandjean, G. J. Long, E. Brück, O. Tegus, N. T. Trung, and K. H. J. Buschow, J. Phys.: Condens. Matter **20**, 475206 (2008).
[49] X. F. Miao, N. V. Thang, L. Caron, H. Yibole, R. I. Smith, N. H. Van Dijk, and E. Brück, Scr. Mater. **124**, 129 (2016).
[50] O. Eriksson and A. Svane, J. Phys.: Condens. Matter **1**, 1589 (1989).
[51] S. A. Brawer, *Relaxation in Viscous Liquids and Glasses* (The American Ceramic Society, Columbus, OH, 1985).
[52] S. A. Brawer, J. Chem. Phys. **81**, 954 (1984).